Review

Journal of RAMAN SPECTROSCOPY

Received: 15 May 2017 Revised: 3 July 2017 Accepted: 16 July 2017 Published online in Wiley Online Library: 13 November 2017

(wileyonlinelibrary.com) DOI 10.1002/jrs.5224

Probing the shear and layer breathing modes in multilayer graphene by Raman spectroscopy

Miao-Ling Lin,[a,b] Jiang-Bin Wu,[a,b] Xue-Lu Liu[a,b] and Ping-Heng Tan[a,b]*

The measurements of interlayer vibrations in multilayer graphene (MLG) have triggered a huge effort to understand phonons, electron–electron, electron–phonon, magneto–phonon interactions and the effect of layer number, stacking sequences, and layer orientations on the Raman spectroscopy of MLG. Here, we provide a review on the optical probe of interlayer vibrations, comprising the shear (C) and layer breathing (LB) modes. At first, we discuss different symmetries of MLGs in AB, ABC, and twisted stacking with an example of trilayer graphene, which dramatically influence the observations of interlayer vibrations. Then a brief description about the physical origins of the C and LB modes is introduced. Finally, two ways are elucidated to probe the interlayer modes in detail. The C and LB modes can be directly probed in the ultralow-wavenumber Raman spectroscopy with special configurations, as depicted by the Raman spectra in MLG with diverse stacking orders. On the other hand, the LB modes can also be derived from the two-phonon overtones in doubly resonant Raman spectra. These approaches can be extended to the other two-dimensional layered materials, which pave the way to measure the interlayer coupling from experiments and thus greatly benefit the future research studies on their fundamental physics and potential applications.

Keywords: multilayer graphene; shear mode; layer breathing mode; ultralow-wavenumber Raman spectroscopy; combination mode

Introduction

The two-dimensional materials (2DMs), including graphene-based materials, h-BN, transition metal chalcogenides (TMDs), and some mixed phases, have attracted much attentions because of their unique optical, electrical, and transport properties.[1] The common feature for these 2DMs is the coexistence of strong in-plane covalent bonding and weak interlayer van der Waals (vdW) force interaction, which makes it easier for them to be mechanically exfoliated from the bulk materials.[2,3] Besides, the few-layer 2DMs can also be grown by chemical vapor deposition (CVD).[4,5] There exist different stacking orders for most 2DMs, such as AB and ABC stacking of graphene-based materials,[6,7] 2H-structure, 3R-structure, and 1T-structure of TMDs,[8] and even the twisted stacking with any twist angle between two adjacent layers,[9–12] giving rise to a wealth of electronic and optical properties.[13,14] In particular, the intriguing properties of single-layer graphene (SLG), such as optical transparency, high mobility (near-ballistic transport), anomalous quantum Hall effect, and the high thermal conductivity, as well as flexibility, robustness, and environmental stability, render it interesting for researchers since it was first discovered in 2004[1] and thus promised as the most prominent candidate in nanoelectronics,[15] optoelectronics,[16] and transparent conducting electrodes.[17,18] These intriguing properties extend to multilayer graphene (MLG). AB-stacked bilayer graphene (BLG) is a tunable band gap semiconductor while AB-stacked trilayer graphene (TLG) has a unique electronic structure consisting, in the simplest approximation, of massless SLG and massive BLG subbands. Few-layer graphene with less than ten layers each shows a distinctive band structure. There is thus an increasing interest in the physics of few-layer graphenes, with or without Bernal stacking, and their applications in useful devices. We use the notation *N*LG to indicate MLG with *N* layers. Thus, 1LG = SLG, 2LG = BLG, 3LG = TLG, and, e.g. 11LG means 11-layer graphene. For a given layer number ($N > 2$), the MLG can exhibit with AB, ABC, and twisted stacking,[11,12,19–22] as shown in Fig. 1, whose electronic and optical properties are influenced by the symmetry breaking and the modified interlayer coupling.[21,23–25] Further, the low-energy electronic properties of MLG and correspondingly, the transport and infrared (IR) optical properties are largely defined by the interactions between the graphene layers. Therefore, the ability to investigate the interlayer coupling and its effects on the electronic band structure or lattice dynamics is at the center of an ever-expanding research area and is critically needed to achieve a detailed understanding of MLG and to expand the potential properties. Besides, vibrational properties and phonon spectra of MLG, including the influence of interlayer coupling on the lattice vibrations, are also of fundamental interest, from which many physical properties (such as thermal conductivity, heat capacity, and shear modulus)[19,26] and quasiparticle dynamics[27] can be derived.

Lattice vibrations, whose quanta are phonons, play an important role in the intriguing properties and experimental phenomena such as thermal conductivity and electrical conductivity in 2DMs. The quantum confinement in atomic scale and the presence of interlayer coupling in multilayer 2DMs result in that their lattice vibrations and phonon spectra are significantly dependent

* *Correspondence to: Ping-Heng Tan, State Key Laboratory of Superlattices and Microstructures, Institute of Semiconductors, Chinese Academy of Sciences, Beijing 100083, China.*
E-mail: phtan@semi.ac.cn

a *State Key Laboratory of Superlattices and Microstructures, Institute of Semiconductors, Chinese Academy of Sciences, Beijing 100083, China*

b *College of Materials Science and Opto-electronic Technology, University of Chinese Academy of Science, Beijing 100049, China*

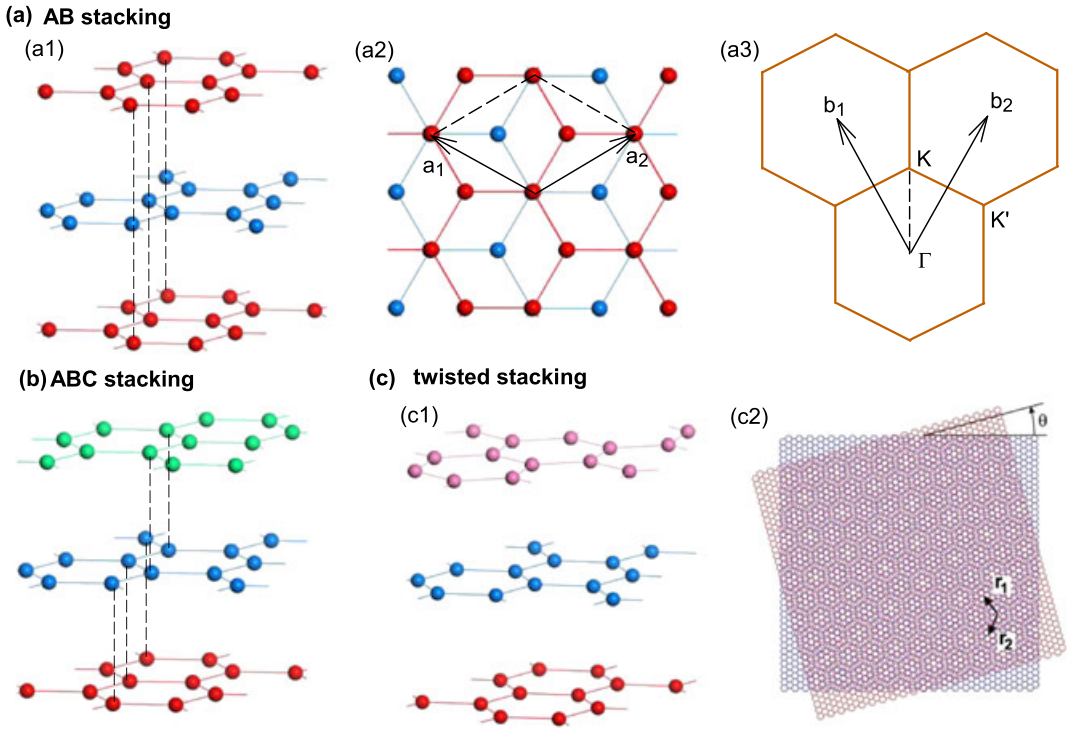

Figure 1. (a)Schematic diagrams of the three-dimensional structure of AB-3LG from the side view (a1), top view (a2), and the corresponding Brillouin zone (a3). $\mathbf{a}_1$ and $\mathbf{a}_2$ in (a2) are basic vectors of the lattice. $\mathbf{b}_1$ and $\mathbf{b}_2$ in (a3) are the basic vectors of the corresponding BZ. *K* and *K′* are the two inequivalent Dirac point while Γ is the zone center. (b) Schematic diagrams of ABC-3LG. (c) Schematic diagrams of *t*(1+2)LG (c1) and the Moiré patterns (c2) formed from the adjacent twisted graphene layers close to the twisted interface with twist angle θ. $\mathbf{r}_1$ and $\mathbf{r}_2$ are the two lattice vectors of the Moiré superlattice.

on the layer number from monolayer to multilayer.[8,28–31] Indeed, there exist two sets of lattice vibrations for multilayer 2DMs: One is the intralayer vibration modes, whose counterparts are also present in the corresponding monolayer and bulk, usually in higher wavenumber region, while the other is the interlayer vibration modes, which originate from the relative motions of the rigid monolayer planes themselves, either perpendicular or parallel to their normal, denoted as the shear (C) modes and the layer breathing (LB) modes, respectively.[12,19,32–34] The shear mode is referred as the *C* mode in MLG because it provides a direct measurement of the interlayer *Coupling* and was first observed in AB-MLG.[19] There are also other denotations[30,33] from different groups for the shear modes, such as S and SM in TMDs and other 2DMs. The vibrational modes especially the interlayer vibrations are also sensitive to the stacking order, interlayer coupling, external perturbations, and the electronic properties.[8,29,30,35,36] MLG can be taken as a typical case for 2DMs to study their *N*-dependent phonons and Raman spectra. Indeed, Raman spectroscopy is one of the most used, nondestructive, and high-resolution tools for characterizing the structure and vibrational properties of carbon-based systems.[28,35–37] A necessary but not sufficient condition for a phonon to be observed is to satisfy the Raman selection rule, in general, to be at the center of Brillouin zone (BZ), Γ, with wavevector q∼0. Usually, two intense peaks at ∼1582 and ∼2700 cm^{-1} can be distinguished in the Raman spectrum of 1LG, which are assigned as degenerate E_{2g} at Γ (the so-called G mode) and overtone phonons in the vicinity of K point (the so-called 2D mode), respectively. As respective to the Raman spectrum of MLG, D, G, and 2D seen in the high-wavenumber (HW) region are due to the in-plane vibrations[38] while the C and LB modes appearing in ultralow-wavenumber (ULW) region are ascribed to the relative motions of the adjacent layers.[11,12,19,39] The C and LB modes are governed by the weak vdW forces, and the corresponding wavenumber (denoted as Pos(C) and Pos(LB), respectively) is lower than 150 cm^{-1}. Thus, it is crucial to take a detailed insight into the C and LB modes before uncovering the interlayer coupling. Furthermore, the observations of interlayer vibrations pave a new way to determine *N* of MLG by the robust *N* dependency of Pos(C) and Pos(LB).[19,31] On the other hand, the stacking orders of MLG can also be accessible by the C and LB modes because the interface interlayer interactions are strongly influenced by its stacking sequences. Moreover, the probe of interlayer vibrations makes it possible to measure the interlayer coupling strength and interface coupling in twisted MLG (*t*MLG),[11,12] which plays an important role in generating its novel electronic, optical, and transporting properties.[7,40–43] Therefore, the experimental probe of the C and LB modes is critically important to reach a fundamental knowledge of the interlayer coupling and thus to have a good control of fancy features for potential applications modulated by the interlayer interactions.

Here, we present a systematic review on the two main ways to measure the C and LB modes of MLG. Firstly, we give a brief introduction about the atomic structures and symmetries of TLG with various stacking orders, which influence the Raman intensities and activities of phonons. Secondly, the physical origins of the C and LB modes are presented using linear chain model (LCM), giving a robust relation between their wavenumber and layer number. Furthermore, the corresponding layer displacement can also be accessible for MLG from LCM. Then, we addressed the Raman measurements of the fundamental C and LB modes in AB-stacked, ABC-stacked, and twisted MLG (denoted as AB-MLG, ABC-MLG, and *t*MLG, also denoted as AB-*N*LG, ABC-*N*LG, and *t*NLG

for the corresponding *N* layer graphene, respectively). Finally, the LB modes can also be derived from their overtones. This review will be helpful to enable a comprehensive understanding of the interlayer coupling in MLG and other two-dimensional layered materials as well as their related heterostructures.

Symmetries of 3LG with various stacking orders

The layer stacking is crucial in defining the symmetries and physical properties of MLG.[25,42,44–46] Here, we take 3LG as an example to illustrate the stacking orders, space group, and the corresponding irreducible representation for phonons at Γ. Schematics in Fig. 1(a–c) show the crystal structures of AB-3LG, ABC-3LG, and *t*3LG, respectively. The bottom two graphene layers are identical to each other for the three stacking orders. The difference between AB-3LG (Fig. 1(a1)) and ABC-3LG (Fig. 1(b)) begins with the third (top) layer. The ABC stacking is also denoted as rhombohedral stacking with reflection symmetry breaking (Fig. 1(b)). From the top view, the top and bottom layers undergo a superposition in ABA stacking, as shown in Fig. 1(a2). $\mathbf{a}_1$ and $\mathbf{a}_2$ are the basic vectors of the unit cell of 3LG. The corresponding BZ can be defined (Fig. 1(a3)) by two basic vectors $\mathbf{b}_1$ and $\mathbf{b}_2$ in which K and K′ are two inequivalent Dirac points at the zone boundary. 1LG belongs to D_{6h} symmetry, and the phonons at Γ can be expressed by $\Gamma_{1LG} = A_{2u} + B_{2g} + E_{1u} + E_{2g}$,[28] comprising three acoustic phonons (A_{2u}+E_{1u}) and three optical phonons (B_{2g}+E_{2g}). The high symmetry (D_{6h}) of 1LG reduced to D_{3h} for AB-3LG while D_{3d} for ABC-3LG, in which the phonons at Γ can be represented by $\Gamma_{AB-3LG} = 2A_1'(R) + 4A_2''(IR) + 4E'(R, IR) + 2E''(R)$ and $\Gamma_{ABC-3LG} = 3(E_g(R) + E_u + A_{1g}(R) + A_{2u}(IR))$, respectively.[47] Correspondingly, taking AB-2LG and ABC-3LG as a basic unit, AB-*N*LG and ABC-*N*LG can be generated, respectively. The odd and even AB-*N*LG with $N > 1$ (*ON*LG and *EN*LG) belongs to D_{3h} and D_{3d} symmetry, and the phonons at BZ center can be expressed by $\Gamma_{ONLG} = (N-1)A_1'(R) + (N+1)A_2''(IR) + (N+1)E'(R, IR) + (N-1)E''$ and Γ_{ENLG}=N(E_g(R)+E_u+A_{1g}(R)+A_{2u}(IR)), respectively. In contrast, ABC-*N*LG always exhibits D_{3d} symmetry.[21] The different point symmetries give various Raman-active modes and thus generate distinguishing Raman spectroscopy.

Particularly, by assembling a *m*LG (AB-*m*LG if $m > 1$) and a *n*LG (AB-*n*LG if $n > 1$) flakes with a twist angle of θ_t between them, a twisted (*m*+*n*)LG (*t*(*m*+*n*)LG) can be formed. *t*MLG can be produced by randomly folding an *m*LG onto an *n*LG during the mechanically exfoliation or alternatively by transferring an *m*LG onto an *n*LG on the SiO_2/Si substrate. It has also been observed to occur in a controlled way of graphene systems grown by CVD[48–50] or other techniques. The choices of the stacking sequences and twist angle θ_t of the interface between two constitutes can result in a great family of twisted systems.[11,12] Considering *t*3LG, there are three typical stacking sequences: *t*(1+2)LG (Fig. 1(c1)), *t*(2+1)LG, and *t*(1+1+1)LG with specific θ_t. Also, the high symmetries in AB-2LG reduce to D_6 or D_3 of *t*(1+1)LG according to its θ_t. The high symmetries in AB-*N*LG and ABC-*N*LG ($N > 2$) also reduce to D_3 of *t*(*n*+*n*)LG ($n > 1$) while C_3 for *t*(*m*+*n*)LG ($m \neq n$),[11] which induces more Raman-active modes, particularly more C and LB modes. Indeed, e.g. in *t*(1+2)LG, all the in-plane vibrations belong to Raman-active E, and the out-of-plane phonons belong to Raman-active A according to its symmetry. Furthermore, the twist angle between two constitutes of *t*(*m*+*n*)LG will generate Moiré patterns, as shown in Fig. 1(c2). The patterns can introduce periodic potential to the crystal lattices and form a superlattice, which profoundly affects the electronic and quantum transport properties of *t*(*m*+*n*)LG by engineering their symmetry and interlayer coupling, such as van Hove singularities (VHSs), renormalized Fermi velocity, mini Dirac points, modified interlayer coupling, and novel vibrational properties.[11–13,45,51–58]

LCM for the C and LB modes in MLG

Before probing the C and LB modes in MLG, it is crucial to figure out their physical origins. In order to illustrate this more clearly, here, we just consider the most stable stacking order, AB stacking in MLG. The two atoms in a unit cell of 1LG lead to six phonon branches, comprising three acoustic (E_{1u} and B_{2g} at Γ) and three optical branches (E_{2g} and B_{2g} at Γ),[59] as discussed previously. In the case of graphite consisting of four atoms in a unit cell, the optical phonons will become Davydov doublets: E_{2g} generates E_{1u}(IR) and E_{2g}(R) whereas B_{2g} goes into an A_{2u}(IR) and a B_{2g}. Furthermore, the acoustic modes at the BZ boundary fold back to the zone center as rigid layer modes: a silent B_{2g} and a Raman-active E_{2g}. The degenerate E_{1u} and the A_{2u} remain as the three acoustic modes. Thus, for graphite, the phonons at Γ are Γ_{bulk}=2(E_{1u}+A_{2u}+E_{2g}+B_{2g}). All these modes and the corresponding vibrational displacements are summarized in Fig. 2, in which the green and purple circles represent the two inequivalent atoms. The HW E_{2g} is the well-known G peak at 1582 cm^{-1} due to the relative motions between the two adjacent atoms in the graphene plane. On the other hand, the Raman-inactive B_{2g} originates from the out-of-plane intralayer vibrations, which is solely measured by the inelastic X-ray scattering[60] or its overtone from the Raman spectroscopy.[61]

Here, we focus on the ULW interlayer modes resulting from the relative vibrations between atoms in the adjacent layers (Fig. 2(c,d)), either parallel or perpendicular to the plane, which has been denoted as C and LB modes, respectively. Considering that the C and LB modes are rigid-layer lattice vibrations, Pos(C) and Pos(LB) can be figured out by regarding each graphene layer in AB-MLG as a single ball so that AB-*N*LG can be simplified as a linear chain with *N* balls in which only nearest-neighbor interlayer interaction can be considered, as shown in Fig. 3(a) for 2-4LG. This is known as LCM. There are *N*-1 degenerated pairs of C modes and *N*-1 LB modes for AB-*N*LG, which are denoted as C_{NN-i} and LB_{NN-i} (i = 1, 2, …, *N*-1), respectively, where the C_{N1} (LB_{N1}) (i.e. $i = N-1$) is the one with highest wavenumber and C_{NN-1} (LB_{NN-1}) (i.e. i = 1) is the one with lowest wavenumber. By assuming that the graphene layers only interact strongly with the nearest adjacent layers and the strength of this coupling per unit area is $\alpha_0^{\parallel}(\alpha_0^{\perp})$ for the C (LB) modes, the wavenumber ω_i (in cm^{-1}) and the displacement patterns of *N*-1 interlayer modes can be calculated by solving the corresponding $N \times N$ (tridiagonal) dynamical matrix as follows[19,62]:

$$\omega_i^2 \mathbf{u}_i = \frac{1}{2\pi^2 c^2 \mu} \mathbf{D} \mathbf{u}_i \quad (1)$$

where $\mathbf{u}_i$ is the phonon eigenvector with the mode i with wavenumber ω_i, μ=7.6×10^{-27}kgÅ^{-2} is the monolayer mass per unit area, c=3.0×10^{10}cm·s^{-1} is the speed of light, and **D**

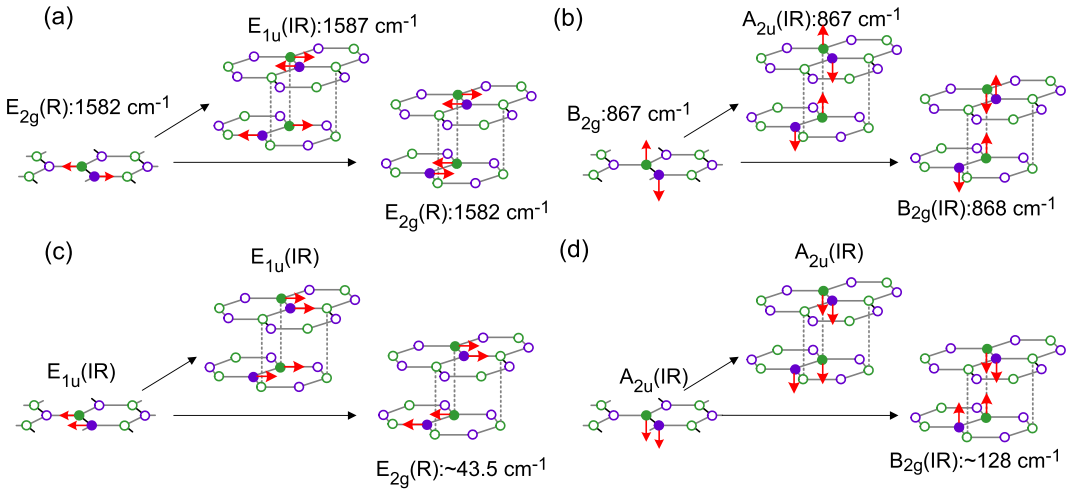

Figure 2. The Γ-point phonons for graphene and graphite: (a) in-plane and (b) out-of-plane HW vibrations, (c) in-plane and (d) out-of-plane acoustic phonons or interlayer vibrations. Green and purple circles represent inequivalent carbon atoms. Red arrows show atom displacements. Black arrows show how each phonon mode in graphene gives rise to two phonon modes of graphite. Their labeling shows Raman-active (R), infrared-active (IR), and inactive (unlabeled) modes.

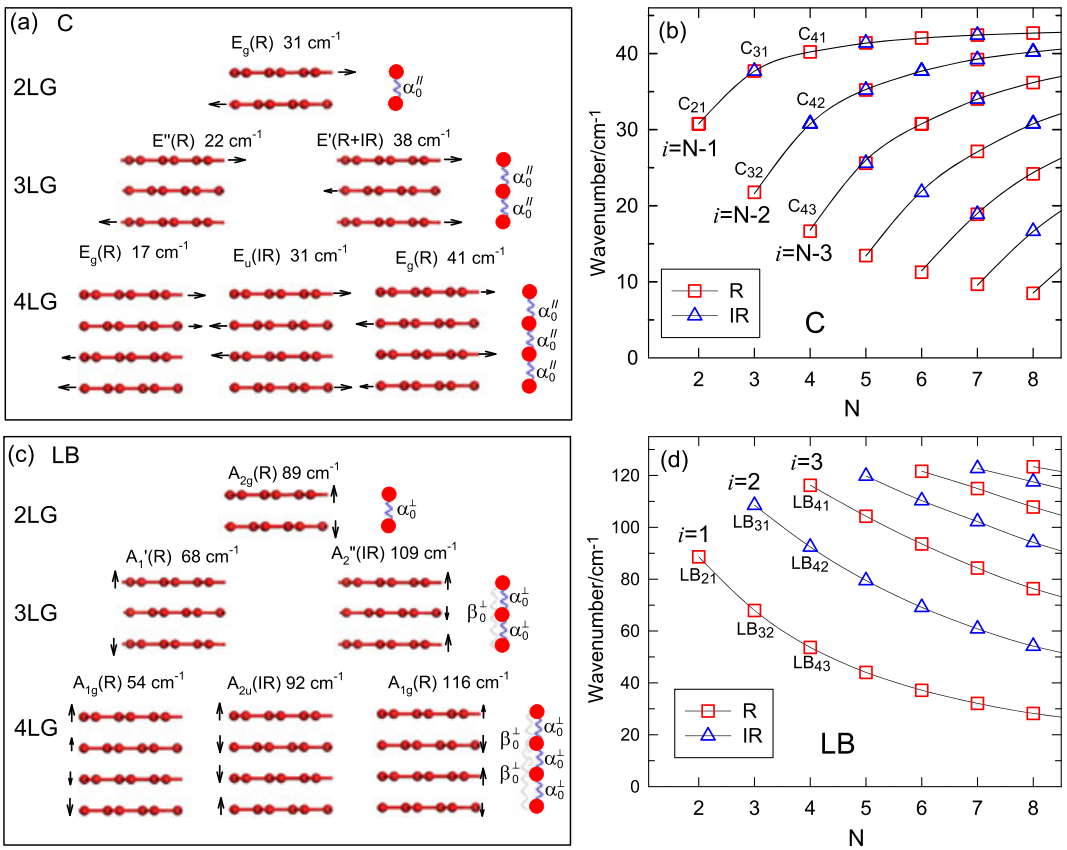

Figure 3. Symmetries, wavenumber, Raman activities, and normal mode displacements for each C modes of AB-stacked 2-4LG (a) and *N*-dependent Pos(C) based on LCM (b). Symmetries, wavenumber, Raman activities, and normal mode displacements for each LB modes of AB-stacked 2-4LG (c) and *N*-dependent Pos(LB) based on 2LCM (d). The rectangles and triangles indicate the Raman (R)-active or infrared (IR)-active modes, respectively. Reproduced with permission from X. Zhang *et al.*[21] Copyright 2016, Elsevier.

the corresponding force constant matrix. Thus, Pos(C_{NN-i}) can be given by

$$Pos(C_{NN-i}) = \frac{1}{\pi c}\sqrt{\alpha_0^{\parallel}/\mu}\,\sin(i\pi/2N) \quad (2)$$

where i=1,2,…, N-1. Accordingly, the i^{th} displacement eigenvector $v_j^{(i)}$ is

$$v_j^{(i)} = \cos[i(2j-1)\pi/2N] \quad (3)$$

where j labels the layers. Moreover, Pos(C_{N1}) can be obtained as follows:

$$Pos(C_{N1}) = \frac{1}{\pi c}\sqrt{\alpha_0^{\parallel}/\mu}\,\cos(\pi/2N) \quad (4)$$

Therefore, the N-dependent Pos(C) and the corresponding atomic displacements can be gained Eqns (2) and (3), as depicted in Fig. 3(a,b). The Raman activity or IR activity of the C modes depends on the symmetry and layer number: N-1 C modes in even and odd layer number MLG can be represented by $\frac{N}{2}E_g$(R)+$\frac{N-2}{2}E_u$(IR) and $\frac{N-1}{2}E''$(R)+$\frac{N-1}{2}E'$(R,IR), respectively. The observed C modes of AB-NLG from experiment at room temperature usually correspond to the i=N-1 branch, which will be discussed later in detail.[19]

It should be noted that, if take N=2, Pos(C_{21})=$\frac{1}{\sqrt{2}\pi c}\sqrt{\alpha_0^{\parallel}/\mu}$. In the case of graphite, $N \to \infty$, Pos(C_{bulk})=$\frac{1}{\pi c}\sqrt{\alpha_0^{\parallel}/\mu}$, that is, $\sqrt{2}$ times as much as Pos(C_{21}). Furthermore, Eqns (2) and (4) can be simplified as follows:

$$Pos(C_{NN-i}) = Pos(C_{bulk})\,\sin(i\pi/2N) \quad (5)$$

$$Pos(C_{N1}) = Pos(C_{bulk})\,\cos(\pi/2N) \quad (6)$$

Similarly, based on Eqns (2) and (4), we can obtain Pos(LB) in AB-NLG just displacing the coupling strength $\alpha_0^{\parallel}$ with $\alpha_0^{\perp}$, which describes the interlayer coupling strength in the perpendicular direction. However, it has been experimentally revealed that some LB modes (LB_{NN-i} with i=1,2,…, N-2) of tMLG undergo lower wavenumber than the LCM results,[12] implying that only nearest-neighbor interlayer interaction is not sufficient to reproduce all the experimental Pos(LB). Wu *et al.* took the second-nearest layer-breathing interactions ($\beta_0^{\perp}$) into account and then solve the corresponding $N\times N$ dynamic matrix; the corresponding wavenumber and atomic displacements for AB-MLG are represented in Fig. 3(c,d). This improved LCM is denoted as 2LCM. Until now, because of the weak electron–phonon coupling (EPC), the LB modes in AB-MLG were solely reported at high temperature by laser heating,[63] which corresponds to i=1 phonon branch. It should be noted that the C and LB modes occur at the ULW region (usually <150 cm^{-1}) because of the weak vdW interaction, which makes it difficult to be probed with the traditional Raman system.

Experimental measurement of the fundamental C and LB modes

The C and LB modes in AB-MLG

With the developments of Raman technologies, now, it is possible to detect the ULW C and LB modes in graphene-based systems. The traditional approach to measure the ULW Raman modes is to use a subtractive mode of double or three cascaded high-resolution monochromators, which provides flexible operations down to 5–10 cm^{-1} at different wavelengths.[64,65] However, this greatly reduces the signal intensity compared with the combination of a single monochromator and a commercial notch or edge filter. Recently, the technical development of the volume-Bragg-grating-based BragGrate notch filter (BNF) has enabled the detection of ULW Raman signals down to 5 cm^{-1} with low excitation power and short accumulation time even just using a single spectrometer.[19] Since then, the new setup is efficient in investigating the ULW interlayer vibrations in 2DMs[11,12,22,32,66–68] as well as the acoustic phonons in nanostructures.[69,70] Recently, the ULW Raman measurements at 488 nm excitation down to 2 cm^{-1} approaching to the Brillouin scattering regions are accessible by using the BNFs with narrow bandwidth and high optical density (OD>4).[71] In particular, the BNFs can also displaced by a special edge filter, with which the modes down to 10 cm^{-1} can be accessible.[72]

Using the Raman setup in combination with BNFs, the C modes of AB-MLG were observed in 2012.[19] Besides, low-doped Si substrate and suspended MLG are also used in this work because the C modes are so weak and likely to be emerged in the high background of Si. Figure 4(a) plots the C mode as well as the G modes of AB-NLG with N ranging from 2 to 8 and of graphite while Fig. 4(b) shows Pos(C) and Pos(G) as a function of 1/N. In contrast to the G peak that remains constant at 1582 cm^{-1}, Pos(C) decreases monotonously with N decreasing. Pos(C_{21})∼31 cm^{-1} of 2LG is $1/\sqrt{2}$ of Pos(C_{bulk})∼43.5 cm^{-1}, in line with the LCM. It is found that Eqn (4) well describes all the experimental data of Pos(C_{N1}), further validating the LCM. By fitting the experimental data, the shear interlayer coupling strength $\alpha_0^{\parallel}$ can be estimated as ∼ 12.8×10^{18} Nm^{-3}, from which the shear modulus (∼4.3 GPa) can be deduced.[19,26] The other C modes in AB-NLG seem to have weaker intensity as a result of weak EPC. Furthermore, all the data are in excellent agreement with the calculations by density functional theory or the previous reports based on force-constant model.[47] In addition, the C modes can be well fitted by Breit–Wigner–Fano lineshape but not by Lorentzian profile, e.g. as shown in Fig. 4(c) in the case of 3LG and bulk graphite. The unusual Breit–Wigner–Fano lineshape can be attributed to the quantum interference between the C mode and a continuum of electronic transitions near the K point.[19]

Although the C modes of AB-MLG have been investigated in detail, the LB modes are seldom reported because of the much weaker EPC or Raman inactivity. It is revealed that by laser heating, the LB modes can be detected because the adsorbates can be removed away at high temperature.[63] However, it is still a challenge to directly probe the LB modes of AB-MLG at room temperature although they have been predicted from the theoretical calculations.[47,73–75]

The C mode in ABC-MLG

Apart from the AB stacking, ABC (rhombohedral) stacking is also common in MLG obtained by mechanical exfoliation from the bulk materials.[20,21] It is found that ∼85% of the sample area corresponds to AB stacking and ∼15% corresponds to ABC stacking,[20] which is consistent with the results from the X-ray diffraction study of graphite.[76] The different symmetry of ABC-NLG (D_{3d}) from AB-NLG leads to its distinct symmetry and Raman activity for C modes. Zhang *et al.* measured ULW Raman spectra of both AB and ABC-stacked MLG at room temperature and found that

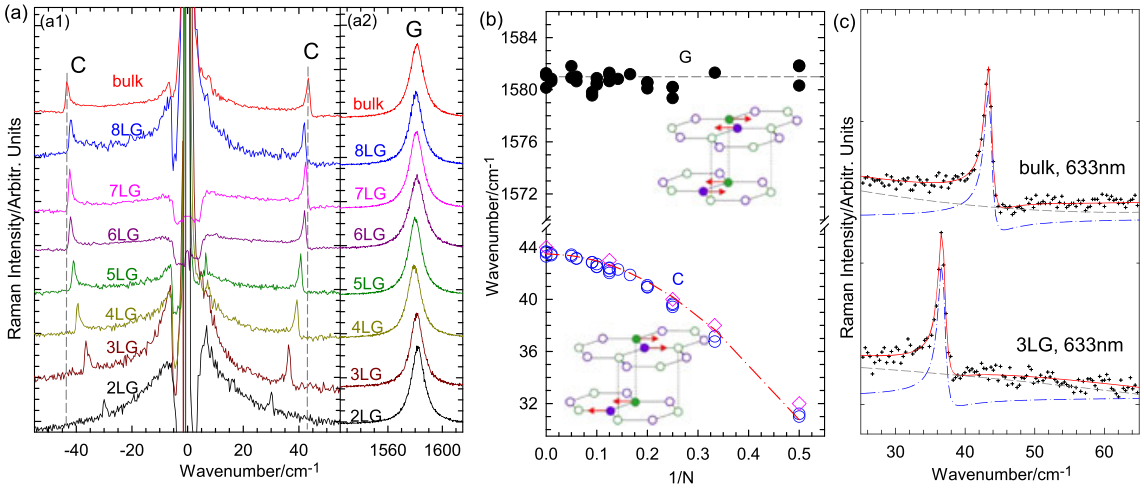

Figure 4. (a) Stokes and anti-Stokes Raman spectra in the region of C (left) and G mode (right) for suspended AB-*N*LG ($2 \leq N \leq 8$) and graphite. The vertical gray dashed line is guide to eyes. (b) Pos(C) (open symbols) and Pos(G) (solid circles) as a function of $1/N$. The dashed lines are calculated by LCM, and the open diamonds are the results form density functional theory while the open circles are from experiments. The horizon gray dashed lines are guides to eyes. The insets show the atomic displacements for C and G modes. (c) The C modes of 3LG and graphite fitted by BWF lineshape for 633 nm excitation. The solid, dashed, and dash-dotted lines are fitted curve, background, and BWF component, respectively. Reproduced with permission from P.-H. Tan *et al.*[19] Copyright 2012, Nature Publishing Group.

weak C_{N1} can only be observed in AB-MLG but not ABC-MLG, as shown in Fig. 5(a). *N*-1 C modes in AB-*N*LG for even and odd *N* are represented by $\frac{N}{2}E_g(R)+\frac{N-2}{2}E_u(IR)$ and $\frac{N-1}{2}(E''(R)+E'(R,IR))$, respectively. According to their Raman tensors, only E_g and E′ can be observed under backscattering configuration. Based on the vibration displacements obtained from LCM (Eqn (3)), the symmetry of each C mode can be assigned. The Raman-activity and IR-activity of each C mode and the corresponding wavenumber in AB-MLG are shown in Fig. 5(b). C_{N1} in AB-*N*LG(E_g) for even *N*, AB-*N*LG(E′) for odd *N* and graphite (E_{2g}) are all Raman-active, which can be experimentally observed.[19,21] However, in ABC-*N*LG, the C modes can be represented by $\frac{N-1}{2}(E_g(R)+E_u(IR))$ in ABC-*N*LG for odd *N* while $\frac{N}{2}E_g(R)+\frac{N-2}{2}E_u(IR)$ in ABC-*N*LG for even *N*. As shown in Fig. 5(c), C_{N1} in ABC-*N*LG (E_g) for even *N* is Raman-active but IR-active in ABC-*N*LG for odd *N*. This implies that in *ON*LG, the stacking order is expected to be distinguished by the C modes but it is not accessible in *EN*LG. However, as shown in Fig. 5(a), the C_{N1} mode cannot be observed in both ABC-3LG and 4LG. The possible reason comes from its small EPC, which is similar to the absence of the other C modes. Thus, the absence of C modes in ABC-MLG can be utilized as a new method to distinguish the AB-stacked and ABC-stacked MLG, bring much convenience to characterize the various stacking order in MLG obtained by mechanical exfoliation from the bulk materials.

Lui *et al.* displaced the Raman spectra of the suspended AB-3LG and ABC-3LG at high temperature of about 800 K by laser heating and found a pronounced peak at 19 cm^{-1} for ABC-3LG, in contrast to the sharp peak at 33 cm^{-1} for AB-3LG.[20] Both peaks are assigned as the C modes, in which the higher-wavenumber C mode is C_{31} and the other is C_{32}. The absence of C_{32} mode in AB-3LG is attributed to the zero intensity under backscattering configuration whereas the disappearance of C_{31} (E_u) in ABC-3LG is owing to the Raman inactivity. In addition, the C and LB modes in MLG with different stacking orders have been also calculated and compared, which suggests that the Raman activities differ from each other for the corresponding mode but the wavenumber is quite the same.[74,75] This is also in line with the experimental results.

The C and LB modes in *t*MLG

Besides AB and ABC stackings, twisted stacking also commonly occurs in graphene-based systems, in particular, for the CVD-grown MLG.[22,77,78] *t*(*m*+*n*)LGs undergo much lower symmetry and interlayer coupling modification, which leads to various vibrational properties, especially for the C and LB modes dependent on the interlayer interactions.[11,12,22,79] θ_t of the *t*(*m*+*n*)LGs can be expressed with the twist vector (p, q), which is defined as the coordinates with respect to the basis vectors of the substitute.[11,41,61] The so-called R and R′ can be used to determine θ_t.[9,11,80] The change of θ_t in *t*MLG results in novel optical properties.[11,12] Indeed, *t*(1+1)LG has parallel electronic bands across the Fermi level, and the energies of the corresponding VHSs depends on θ_t.[11,43,45,55,57,81] The electronic structure of *t*(*m*+*n*)LG is also closely related with θ_t and those of substituents.[11,66] The Raman intensity of the C, LB, and G modes is significantly enhanced in *t*(*m* + *n*)LGs for specific excitation energies.[11,12,22] Fig. 6(a) plots the Raman spectra in the region of C and G modes of four *t*(*m*+*n*)LGs resonantly excited by specific energies (E_{ex}), which are normalized by the corresponding G mode intensity, I(G). Closer inspection shows that the G band consists of two sub-bands if *m* or $n > 1$, which we call G^- and G^+, using a similar terminology to that used in strained graphene. It shows that I(C), I(G^-), and I(G^+) are very sensitive to E_{ex}, exhibiting a significant resonant behavior. This behavior is assigned to the resonance between VHSs in the joint density of states of all optically allowed transitions ($JDOS_{OAT}$) in *t*(*m*+*n*)LGs and the laser excitation energy.[11,82–84] The resonant profiles of I(C), I(G^-) and I(G^+) can be as wide as several hundreds of meV, dependent on the profile of $JDOS_{OAT}$. Figure 6(b) shows the band structure of *t*(1+3)LG with θ_t=10.6° . The resonant profiles of I(C_{31}) and I(C_{32}) of the *t*(1+3)LG depicted in Fig. 6(c) are closely related with the corresponding $JDOS_{OAT}$.

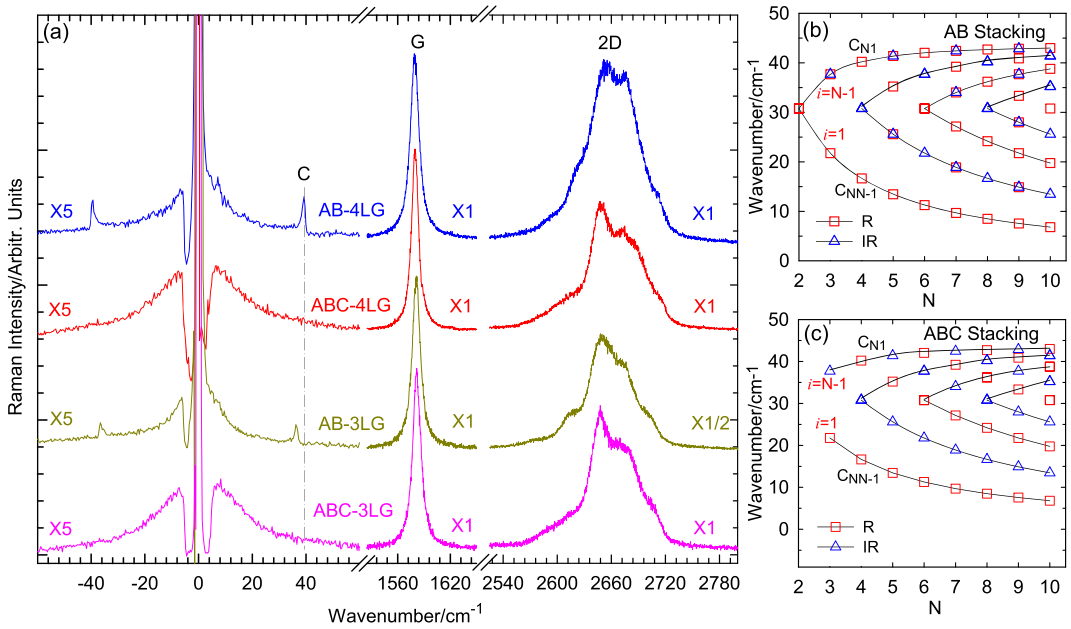

Figure 5. (a) Raman spectra of AB-3LG and ABC-3LG, and 4LG in the region of C, G, and 2D modes. The positions and Raman-activities or infrared-activities of C modes for AB-MLG (b) and ABC-MLG (c) as a function of *N*. Reproduced with permission from X. Zhang *et al.*[21] Copyright 2016, Elsevier.

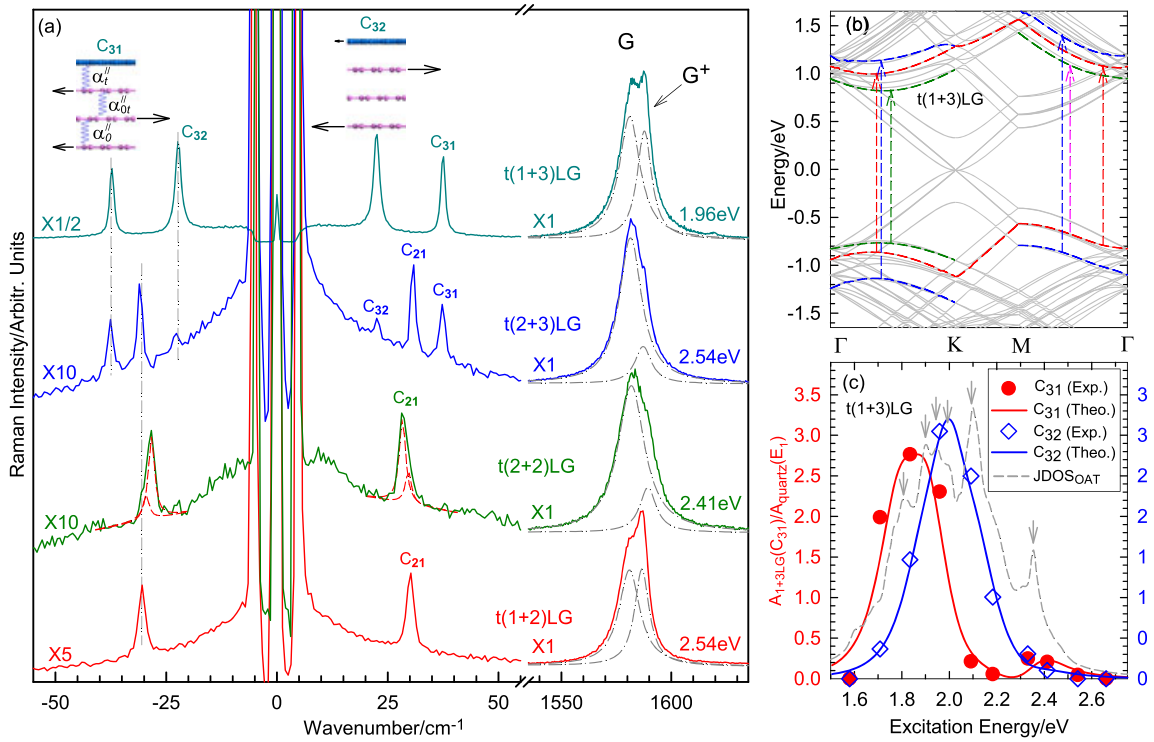

Figure 6. (a) Stokes/anti-Stokes Raman spectra in the region of C modes and Stokes spectra in the G spectral region for four *t*(*m*+*n*)LG. The excitation energy for each sample is indicated. The spectra are scaled and offset for clarity. The scaling factors of the individual spectra are also shown. (b) The band structure of *t*(1+3)LG with θ_t=10.6° . Some typical transitions are highlighted by vertical dashed lines. (c) The experimental areas A(C_{31}) and A(C_{32}) as a function of E_{ex}. The symbols (open and filled) show the experimental data while the solid lines are from simulations. The gray dashed line shows $JDOS_{OAT}$ in *t*(1+3)LG, in which the VHSs are indicated by arrows. Reproduced with permission from J.-B. Wu *et al.*[11] Copyright 2014, Nature Publishing Group.

Figure 6(a) clearly demonstrates that the observed C modes in *t*(*m*+*n*)LG are related to the shear vibrations of the constituent AB-*m*LG and AB-*n*LG, but not to the (*m*+*n*)LG. If $m \neq n$, e.g., in the *t*(2+3)LG, C_{31} and C_{32} of the 3LG constituent and C_{21} of the 2LG constituent are observed. If $m = n$, e.g. in the *t*(2+2)LG, a broad and asymmetrical C_{21} peak had been observed,[11] which can be fitted using two Lorentzians C_{21}^{-} and C_{21}^{+}. This splitting is known as Davydov splitting,[85] which results from the Davydov splitting between two equivalent 2LG constituents.[11] The Davydov splitting is also expected in all *t*(*n*+ *n*)LG as well as the HW Raman modes of other multilayer 2DMs.[86–91] All these fancy features indicates that the interface coupling ($\alpha_t^{\parallel}$) between two constitutes is much smaller than that in AB-MLG ($\alpha_0^{\parallel}$) or the perturbed force constant adjacent to the interface ($\alpha_{0t}^{\parallel}$), as shown in the insets of Fig. 6(a). The averages of $\alpha_t^{\parallel}$ and $\alpha_{0t}^{\parallel}$ are estimated 2.4×10^{18} Nm^{-3} and 11.8×10^{18} Nm^{-3}, which are decreased by $\sim$ 9% and $\sim$80% with respect to $\alpha_0^{\parallel}$, respectively, but both are insensitive to the twist angle θ_t. Accordingly, the mode displacements are mainly localized within the AB-*n*LG or AB-*m*LG constitutes and only weakly affected by the coupling across the twisted interface, as shown in the insets of Fig. 6(a). The softening of the C modes and the reduction of the restore forces in *t*MLG are revealed to be due to the periodicity mismatch at the twisted interface.[12]

In contrast, the LB modes are revealed to be dependent on the total layer number (*N*) of *t*NLG, but not on its constituents, as depicted in Fig. 7(a). It should be noted here that the LB modes shown in Fig. 7(a) are significantly resonant because the excitation laser energies are matching with the VHSs in the $JDOS_{OAT}$. In contrast to the C modes appearing at both XX and XY configurations,[92] the LB modes vanish in the XY configuration. Follow this tendency, it is easy to distinguish the LB modes from the C modes. A pronounced LB peak exits at 116 cm^{-1} for *t*(1+3)LG, close to LB_{41}. The resemble behaviors are observed in all the *t*(*m*+*n*)LG; e.g., the *t*(2+2)LG sample shows a

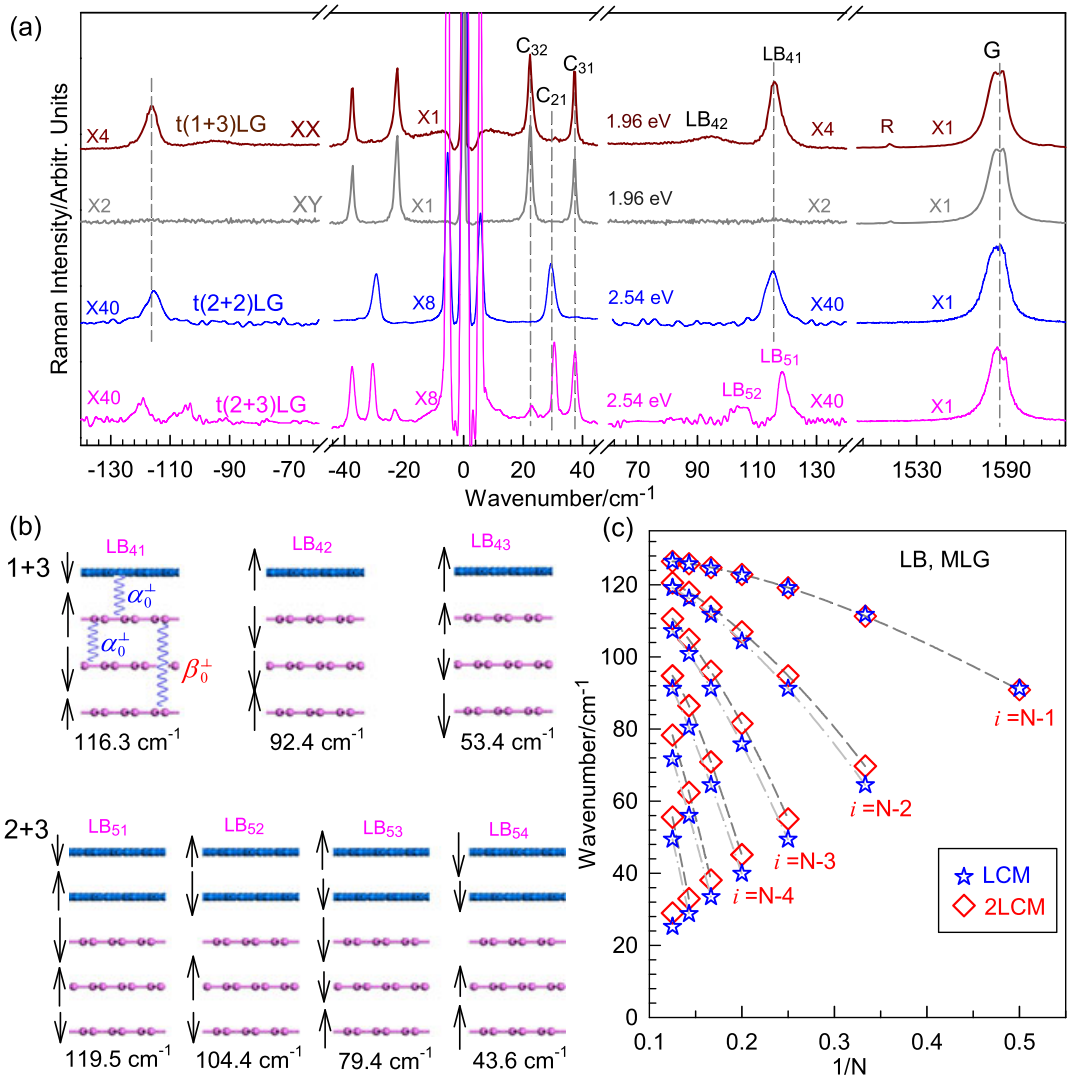

Figure 7. (a) Stokes/anti-Stokes Raman spectra in the region of C and LB modes and Stokes spectra in the G spectral region for four *t*(*m*+*n*)LG. Polarized spectra of *t*(1+3)LG are also shown. The excitation energy for each sample is indicated. All the spectra are scaled and offset for clarity. The scaling factors of the individual spectra are also shown. (b) Normal mode displacements and wavenumber for *t*(1+3)LG and *t*(2+3)LG from 2LCM. The schematic of 2LCM is also shown. (c) The theoretical wavenumber of the LB modes as a function of *N* calculated from LCM and 2LCM. The gray dashed-dotted and dashed lines are guides to the eyes for LCM and 2LCM, respectively. Blue crosses show the experimental (exp) data. Reproduced with permission from J.-B. Wu *et al.*[12] Copyright 2015, American Chemical Society.

LB_{41} mode at ~115.5 cm^{-1}, whose position is almost identical to that of *t*(1+3)LG. This means that the LB modes in *t*MLG are not localized inside its constituents but are a collective motion involving all layers. This is ascribed to the similar charge density at the twisted and Bernal stacked interfaces, which governs the interlayer layer-breathing interactions.[12] Based on LCM and experimental Pos(LB_{N1}), $\alpha_0^{\perp}$ in *t*MLG can be estimated as 106×10^{18} Nm^{-3}, quite close to the theoretical value of Bernal stacked interfaces.[12] The corresponding layer displacements are also shown in Fig. 7(b). However, the simulated Pos(LB_{42}) and Pos(LB_{52}) based on LCM (Fig. 7(c)) are 4.3 and 2.9 cm^{-1} lower than those observed in *t*(1+3)LG and *t*(2+3)LG (Fig. 7(a)), respectively. It suggests that the θ_t-independent second-nearest-neighbor layer-breathing interactions ($\beta_0^{\perp}$) is necessary to be considered to fit the experimental values of Pos(LB_{42}) and Pos(LB_{52}). The new model is denoted as 2LCM and $\beta_0^{\perp} \sim 9.3 \times 10^{18}$ Nm^{-3} well fits all the experimental data (crosses in Fig. 7(c)). Figure 7(c) demonstrates the different Pos(LB) estimated by LCM and 2LCM along with the experimental data. Because the relative motions of the second-nearest-neighbor layers are always out-of-phase for LB_{N2}, so $\alpha_0^{\perp}$ with additional $\beta_0^{\perp}$ is crucial to reproduce their wavenumber. However, the second-nearest-neighbor layers are always in-phase for LB_{N1}; therefore, Pos(LB_{N1}) is insensitive to $\beta_0^{\perp}$, and it can be estimated by LCM. Besides, all the fitting data and observed wavenumber for the C and LB modes in *t*MLG can also be confirmed by the calculations from density functional theory, as indicated by Wu *et al*.

Different behaviors of Pos(C) and Pos(LB) in *t*MLG make it easy to characterize the layer number and stacking sequences of *t*MLG with interlayer vibrations. Lin *et al*.[93] have developed a systematical method to distinguish the stacking orders of *t*MLGs grown by CVD. The LB modes are helpful to identify the total layer number of *t*MLG, while the C modes provide one convenient method to determine the stacking sequence of the constituents in *t*MLG. Furthermore, the twist angle of the twisted interfaces in *t*MLG can also be ascertained by the wavenumber of R modes, which originates from TO phonons with finite wavevector selected by the twist wave vector. The reliable way to identify the stacking orders advances an important step for the characterization of *t*MLGs, in particular, for CVD-grown MLGs, and thus paving way of tailoring the properties of *t*MLGs with specific stacking order on demand.

Probing the LB modes via their overtones

Other than the direct way to measure interlayer vibrations, the LB modes can also be accessible through the two-phonon overtone (2ZO′) spectra in double-resonant Raman spectroscopy.[94] ZO′ phonon branches are usually used to describe the relative displacements of the individual graphene plane in the perpendicular direction. Thus, LB modes can be considered as the ZO′ phonon at the BZ center. ZO′ phonon branches are observable

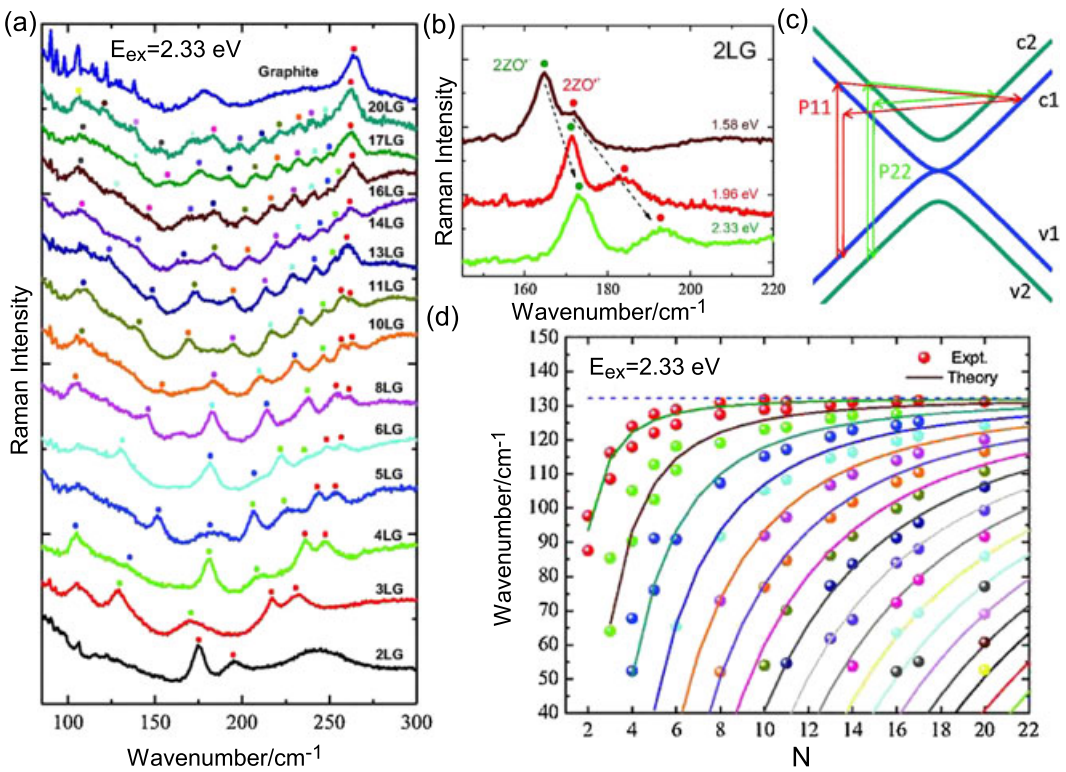

Figure 8. (a) The Raman spectra in the region of 2ZO′ modes for (2-20)LG and graphite with 2.33 eV excitation. The peaks indicated by the symbols with the same color are the subpeaks from the same $ZO'^{(n)}_N$ branch. (b) Normalized 2ZO′ spectra of 2LG with 1.58, 1.96, and 2.33 eV excitations. The high-wavenumber and low-wavenumber components of the 2ZO′ band are denoted as $2ZO'^{+}$ and $2ZO'^{-}$, respectively. (c) The main electronic scattering processes in the two-phonon double-resonance Raman mechanism of the 2ZO′ mode in 2LG. The $2ZO'^{+}$ and $2ZO'^{-}$ peaks are ascribed to the P11 and P22 processes, respectively. (d) The wavenumber of ZO′ obtained from the overtone Raman peaks in (a), as a function of *N*, whose frequencies are half of the $2ZO^{-}$ and $2ZO^{+}$ reported in (a). The experimental results (symbols) are compared with the LCM results (lines). The dashed line denotes the wavenumber of ZO′ in graphite. Reproduced with permission from C.-H. Lui *et al*.[94] Copyright 2013, American Physical Society.

because of the intravalley double resonance process. Similar to the LO±ZO′ combination modes, 2ZO′s are also sensitive to *N*. For suspended AB-*N*LG with *N* ranging from 2 to 20, 2ZO′ are seen over the spectral range of 80–300 cm^{-1}, as depicted in Fig. 8(a), whose features arise from each of the different LB vibrations with finite wave vectors. With increasing *N*, the number of 2ZO′ Raman peaks grows systematically, and the spectral shape of the whole band gradually approaches that of the graphite spectrum, highlighting the remarkable sensitivity of the LB modes to layer number. In principle, there should be a single LB mode for 2LG. However, two peaks can be distinguished in a wavenumber range of ~180 cm^{-1} (Fig. 8(b)) although their intensity is 100 times weaker than that of the G mode. Furthermore, the peaks blueshift and the two components separating more widely from one another as the laser excitation energy increases from 1.58 to 2.33 eV. The strong dispersive Raman response further confirms a intravalley double resonant Raman process. The ZO modes with specific wavevector can be activated by a given laser energy. The two Raman peaks, $2ZO'^{-}$ for the low-wavenumber peak while $2ZO'^{+}$ for HW peak can be elucidated with two intravalley double-resonant Raman scattering processes, as shown in Fig. 8(c). Pos(ZO′) at Γ corresponding to LB modes in 2LG can be extrapolated to be ~90 cm^{-1}, which is comparable with the theoretical predictions and other experiments.[79] Accordingly, the discussion can be extended to AB-*N*LG. The interlayer coupling will create *N*-1 distinct ZO′ branches with finite wavenumbers at Γ for AB-*N*LG, which can be denoted as $ZO'^{(n)}_N$ with *n*=1,2,…,*N*-1 and $ZO'^{(1)}_N$ represent the highest-frequency branch. The Raman spectra of suspended MLG with layer number from 2 to 20 are examined, and a panoply of Raman peaks is observed in the range of 80–300 cm^{-1}. All the ZO′ branches for each layer from LCM are depicted with the solid lines while the symbols represent the Pos($ZO'^{(n)}_N$) from experiment. The theoretical results provide an excellent overall fit to the experimental data for all *N* (Fig. 8(d)).

All the data demonstrated that the interlayer vibrations and coupling in MLG can be probed via two-phonon overtone Raman features. The *N*-dependent behavior of interlayer vibrations can be well expressed within LCM. In addition, the LB modes can be derived from the combination modes (LO±ZO′).[39,95] Lui *et al.* also addressed the *N*-dependent LO+ZO′ using the nearest-neighbor hamonic couplings,[39] which are well fitted with the experimental data. Furthermore, LO+ZO′ exhibits stacking-order-dependent behavior; e.g. for AB-stacked samples, there are several peaks in the region of LO+ZO′ (~1750 cm^{-1}), and the peak at the highest wavenumber is significantly stronger than the other subpeaks; on the other hand, ABC-stacked MLG exhibits with greater number of peaks with narrower line widths and more evenly distributed spectral weight than the spectra AB-MLG. This suggests that LO+ZO′ can also used to distinguish the different stacking orders. However, in the way of studying LB modes through LO±ZO′ combination modes, it is a little difficult to precisely extract Pos(LB). Compared with the direct way to measure the fundamental C and LB modes, the deduced ZO′ modes here through the combinations or overtones (2ZO′) are not the LB modes at Γ but with a finite wave vector away from the LB modes selected by double-resonant Raman scattering process. Thus, a minor error (~ 2 cm^{-1}) is expected from the in-plane phonon dispersion of the phonon branch related the LB modes at Γ.

Conclusion

The MLG as well as the related heterostructures are coupled with the weak vdW interactions, resulting in novel optical and electronic properties governed by the interlayer coupling. The C and layer LB modes are due to relative motions of the planes, either perpendicular or parallel to their normal, allowing one to directly probe the interlayer interactions in MLG. Here, we reviewed the way to probe the C and LB modes in MLG via Raman spectroscopy, which is highly sensitive to *N* and stacking order. Only the highest-wavenumber C modes in AB-MLG can be measured at room temperature whereas the LB modes is reported to be activated by laser heating. However, neither the C nor LB modes can be detected at room temperature for ABC-stacked MLG. Furthermore, the VHSs of *t*MLG provide a new way to probing more C and LB modes by resonant Raman spectroscopy. For *tN*LG (with $N = m+n$), the observed C modes follow those of AB-stacked *m*(*n*)LG while the LB modes follow those of AB-stacked *N*LG. On the other hand, in contrast to the direct way to measure the C and LB modes, the LB modes can be also distinguished through the two-phonon overtones (2ZO′). Raman spectroscopy is expected to be an effective tool to characterize the interlayer coupling, layer number, stacking order as well as other physical properties for graphene-related systems and vdW heterostructures. This review will uncover the interlayer vibrations of MLG and their hybrids or heterostructures, thus shedding light on their potential applications.

Acknowledgements

We acknowledge support from the National Key Research and Development Program of China grant no. 2016YFA0301204 and the National Natural Science Foundation of China (11434010, 11474277, 11225421), and Beijing Municipal Science and Technology Commission..

References

[1] A. K. Geim, K. S. Novoselov, The rise of graphene, *Nat. Mater.* **2007**, *6*, 183.
[2] K. S. Novoselov, A. K. Geim, S. V. Morozov, D. Jiang, Y. Zhang, S. V. Dubonos, I. V. Grigorieva, A. A. Firsov, Electric field effect in atomically thin carbon films, *Science* **2004**, *306*, 666.
[3] K. S. Novoselov, D. Jiang, F. Schedin, T. J. Booth, V. V. Khotkevich, S. V. Morozov, A. K. Geim, Two-dimensional atomic crystals, *Proc. Natl. Acad. Sci. USA* **2005**, *102*, 10451.
[4] X. Li, W. Cai, J. An, S. Kim, J. Nah, D. Yang, R. Piner, A. Velamakanni, I. Jung, E. Tutuc, S. K. Banerjee, L. Colombo, R. S. Ruoff, Large-area synthesis of high-quality and uniform graphene films on copper foils, *Science* **2009**, *324*, 1312.
[5] Y.-H. Lee, X.-Q. Zhang, W. Zhang, M.-T. Chang, C.-T. Lin, K.-D. Chang, Y.-C. Yu, J. T.-W. Wang, C.-S. Chang, L.-J. Li, T.-W. Lin, Synthesis of large-area mos2 atomic layers with chemical vapor deposition, *Adv. Mater.* **2012**, *24*, 2320.
[6] F. Zhang, B. Sahu, H. Min, A. H. MacDonald, Band structure of *ABC*-stacked graphene trilayers, *Phys. Rev. B* **2010**, *82*, 035409.
[7] M. Koshino, Interlayer screening effect in graphene multilayers with *aba* and *abc* stacking, *Phys. Rev. B* **2010**, *81*, 125304.
[8] X. Zhang, X.-F. Qiao, W. Shi, J.-B. Wu, D.-S. Jiang, P.-H. Tan, Phonon and Raman scattering of two-dimensional transition metal dichalcogenides from monolayer, multilayer to bulk material, *Chem. Soc. Rev.* **2015**, *44*, 2757.
[9] V. Carozo, C. M. Almeida, E. H. M. Ferreira, L. G. Cançado, C. A. Achete, A. Jorio, Raman signature of graphene superlattices, *Nano Lett.* **2011**, *11*, 4527.
[10] S. Huang, X. Ling, L. Liang, J. Kong, H. Terrones, V. Meunier, M. S. Dresselhaus, Probing the interlayer coupling of twisted bilayer mos2 using photoluminescence spectroscopy, *Nano Lett.* **2014**, *14*, 5500.

[11] J.-B. Wu, X. Zhang, M. Ijäs, W.-P. Han, X.-F. Qiao, X.-L. Li, D.-S. Jiang, A. C. Ferrari, P.-H. Tan, Resonant Raman spectroscopy of twisted multilayer graphene, *Nat. Commun.* **2014**, *5*, 5309.
[12] J.-B. Wu, Z.-X. Hu, X. Zhang, W.-P. Han, Y. Lu, W. Shi, X.-F. Qiao, M. Ijiäs, S. Milana, W. Ji, A. C. Ferrari, P.-H. Tan, Interface coupling in twisted multilayer graphene by resonant Raman spectroscopy of layer breathing modes, *ACS Nano* **2015**, *9*, 7440.
[13] K. S. Kim, A. L. Walter, L. Moreschini, T. Seyller, K. Horn, E. Rotenberg, A. Bostwick, Coexisting massive and massless Dirac fermions in symmetry-broken bilayer graphene, *Nat. Mater.* **2013**, *12*, 887.
[14] T. Jiang, H. Liu, D. Huang, S. Zhang, Y. Li, X. Gong, Y.-R. Shen, W.-T. Liu, S. Wu, Valley and band structure engineering of folded mos_2 bilayers, *Nat. Nanotechnol.* **2014**, *9*, 6825.
[15] Y.-M. Lin, C. Dimitrakopoulos, K. A. Jenkins, D. B. Farmer, H.-Y. Chiu, A. Grill, P. Avouris, 100-ghz transistors from wafer-scale epitaxial graphene, *Science* **2010**, *327*, 662.
[16] F. Bonaccorso, Z. Sun, T. Hasan, A. C. Ferrari, Graphene photonics and optoelectronics, *Nat. Photon.* **2010**, *4*, 611.
[17] K. S. Kim, Y. Zhao, H. Jang, S. Y. Lee, J. M. Kim, K. S. Kim, J.-H. Ahn, P. Kim, J.-Y. Choi, B. H. Hong, Large-scale pattern growth of graphene films for stretchable transparent electrodes, *Nature* **2009**, *457*, 706.
[18] S. Bae, H. Kim, Y. Lee, X. Xu, J.-S. Park, Y. Zheng, J. Balakrishnan, T. Lei, H. Ri Kim, Y. I. Song, Y.-J. Kim, K. S. Kim, B. Ozyilmaz, J.-H. Ahn, B. H. Hong, S. Iijima, Roll-to-roll production of 30-inch graphene films for transparent electrodes, *Nat. Nanotechnol.* **2010**, *5*, 574.
[19] P.-H. Tan, W.-P. Han, W.-J. Zhao, Z.-H. Wu, K. Chang, H. Wang, Y.-F. Wang, N. Bonini, N. Marzari, N. Pugno, G. Savini, A. Lombardo, A. C. Ferrari, The shear mode of multilayer graphene, *Nat. Mater.* **2012**, *11*, 294.
[20] C. H. Lui, Z. Ye, C. Keiser, E. B. Barros, R. He, Stacking-dependent shear modes in trilayer graphene, *Appl. Phys. Lett.* **2015**, *106*, 041904.
[21] X. Zhang, W.-P. Han, X.-F. Qiao, Q.-H. Tan, Y.-F. Wang, J. Zhang, P.-H. Tan, Raman characterization of AB- and ABC-stacked few-layer graphene by interlayer shear modes, *Carbon* **2016**, *99*, 118.
[22] J.-B. Wu, H. Wang, X.-L. Li, H. Peng, P.-H. Tan, Raman spectroscopic characterization of stacking configuration and interlayer coupling of twisted multilayer graphene grown by chemical vapor deposition, *Carbon* **2016**, *110*, 225.
[23] C. H. Lui, Z. Li, K. F. Mak, E. Cappelluti, T. F. Heinz, Observation of an electrically tunable band gap in trilayer graphene, *Nat. Phys.* **2011**, *7*, 944.
[24] K. F. Mak, J. Shan, T. F. Heinz, Electronic structure of few-layer graphene: experimental demonstration of strong dependence on stacking sequence, *Phys. Rev. Lett.* **2010**, *104*, 176404.
[25] H. Schmidt, J. C. Rode, D. Smirnov, R. J. Haug, Superlattice structures in twisted bilayers of folded graphene, *Nat. Commun.* **2014**, *5*, 5742.
[26] X. Zhang, Q.-H. Tan, J.-B. Wu, W. Shi, P.-H. Tan, Review on the Raman spectroscopy of different types of layered materials, *Nanoscale* **2016**, *8*, 6435.
[27] A. Bostwick, T. Ohta, T. Seyller, K. Horn, E. Rotenberg, Quasiparticle dynamics in graphene, *Nat. Phys.* **2007**, *3*, 36.
[28] A. C. Ferrari, D. M. Basko, Raman spectroscopy as a versatile tool for studying the properties of graphene, *Nat. Nanotechnol.* **2013**, *8*, 235.
[29] X. Lu, X. Luo, J. Zhang, S. Y. Quek, Q. Xiong, Lattice vibrations and Raman scattering in two-dimensional layered materials beyond graphene, *Nano Res.* **2016**, *9*, 3559.
[30] J. Ji, S. Dong, A. Zhang, Q. Zhang, Low-frequency interlayer vibration modes in two-dimensional layered materials, *Phys. E* **2016**, *80*, 130.
[31] X.-L. Li, W.-P. Han, J.-B. Wu, X.-F. Qiao, J. Zhang, P.-H. Tan, Layer-number dependent optical properties of 2D materials and their application for thickness determination, *Adv. Funct. Mater.* **2017**, *27*, 1604468.
[32] X. Zhang, W.-P. Han, J.-B. Wu, S. Milana, Y. Lu, Q.-Q. Li, A. C. Ferrari, P.-H. Tan, Raman spectroscopy of shear and layer breathing modes in multilayer mos_2, *Phys. Rev. B* **2013**, *87*, 115413.
[33] Y. Zhao, X. Luo, H. Li, J. Zhang, P. T. Araujo, C. K. Gan, J. Wu, H. Zhang, S. Y. Quek, M. S. Dresselhaus, Q. Xiong, Interlayer breathing and shear modes in few-trilayer mos_2 and wse_2, *Nano Lett.* **2013**, *13*, 1007.
[34] H. Zeng, B. Zhu, K. Liu, J. Fan, X. Cui, Q. M. Zhang, Low-frequency Raman modes and electronic excitations in atomically thin MoS_2 films, *Phys. Rev. B* **2012**, *86*, 241301.
[35] A. C. Ferrari, Raman spectroscopy of graphene and graphite: Disorder, electron-phonon coupling, doping and nonadiabatic effects, *Solid State Commun.* **2007**, *143*, 47.
[36] L. M. Malard, M. A. Pimenta, G. Dresselhaus, M. S. Dresselhaus, Raman spectroscopy in graphene, *Phys. Rep.* **2009**, *473*, 51.
[37] A. Jorio, M. S. Dresselhaus, R. Saito, G. F. Dresselhaus, *Raman Spectrocopy in Graphene-related Systems*, Wiley-VCH, Weinheim, Germany, **2011**.
[38] A. C. Ferrari, J. C. Meyer, V. Scardaci, C. Casiraghi, M. Lazzeri, F. Mauri, S. Piscanec, D. Jiang, K. S. Novoselov, S. Roth, A. K. Geim, Raman spectrum of graphene and graphene layers, *Phys. Rev. Lett.* **2006**, *97*, 187401.
[39] C. H. Lui, L. M. Malard, S. Kim, G. Lantz, F. E. Laverge, R. Saito, T. F. Heinz, Observation of layer-breathing mode vibrations in few-layer graphene through combination Raman scattering, *Nano Lett.* **2012**, *12*, 5539.
[40] A. Yacoby, Graphene: tri and tri again, *Nat. Phys.* **2011**, *7*, 925.
[41] G. Trambly de Laissardière, D. Mayou, L. Magaud, Localization of Dirac electrons in rotated graphene bilayers, *Nano Lett.* **2010**, *10*, 804.
[42] W. Bao, L. Jing, J. Velasco, Y. Lee, G. Liu, D. Tran, B. Standley, M. Aykol, S. B. Cronin, D. Smirnov, M. Koshino, E. McCann, M. Bockrath, C. N. Lau, Stacking-dependent band gap and quantum transport in trilayer graphene, *Nat. Phys.* **2011**, *7*, 948.
[43] K. Kim, S. Coh, L. Z. Tan, W. Regan, J. M. Yuk, E. Chatterjee, M. F. Crommie, M. L. Cohen, S. G. Louie, A. Zettl, Raman spectroscopy study of rotated double-layer graphene: misorientation-angle dependence of electronic structure, *Phys. Rev. Lett.* **2012**, *108*, 246103.
[44] A. Kumar, W. Escoffier, J. M. Poumirol, C. Faugeras, D. P. Arovas, M. M. Fogler, F. Guinea, S. Roche, M. Goiran, B. Raquet, Integer quantum hall effect in trilayer graphene, *Phys. Rev. Lett.* **2011**, *107*, 126806.
[45] G. Li, A. Luican, J. M. B. Lopes dos Santos, A. H. Castro Neto, A. Reina, J. Kong, E. Y. Andrei, Observation of van Hove singularities in twisted graphene layers, *Nat. Phys.* **2010**, *6*, 109.
[46] J. Campos-Delgado, L. G. Cançado, C. A. Achete, A. Jorio, J.-P. Raskin, Raman scattering study of the phonon dispersion in twisted bilayer graphene, *Nano Res.* **2013**, *6*, 269.
[47] H. Wang, Y. F. Wang, X. W. Cao, M. Feng, G. X. Lan, Vibrational properties of graphene and graphene layers, *J. Raman. Spectrosc.* **2009**, *40*, 1791.
[48] J. T. Robinson, S. W. Schmucker, C. B. Diaconescu, J. P. Long, J. C. Culbertson, T. Ohta, A. L. Friedman, T. E. Beechem, Electronic hybridization of large-area stacked graphene films, *ACS Nano* **2013**, *7*, 637.
[49] J. Campos-Delgado, G. Algara-Siller, C. N. Santos, U. Kaiser, J.-P. Raskin, Twisted bi-layer graphene: microscopic rainbows, *Small* **2013**, *9*, 3247.
[50] Y. Song, D. Pan, Y. Cheng, P. Wang, P. Zhao, H. Wang, Growth of large graphene single crystal inside a restricted chamber by chemical vapor deposition, *Carbon* **2015**, *95*, 1027.
[51] Z. Ni, Y. Wang, T. Yu, Y. You, Z. Shen, Reduction of fermi velocity in folded graphene observed by resonance Raman spectroscopy, *Phys. Rev. B* **2008**, *77*, 235403.
[52] S. Shallcross, S. Sharma, O. A. Pankratov, Quantum interference at the twist boundary in graphene, *Phys. Rev. Lett.* **2008**, *101*, 056803.
[53] D. S. Lee, C. Riedl, T. Beringer, A. H. Castro Neto, K. von Klitzing, U. Starke, J. H. Smet, Quantum hall effect in twisted bilayer graphene, *Phys. Rev. Lett.* **2011**, *107*, 216602.
[54] R. Bistritzer, A. H. MacDonald, Moiré bands in twisted double-layer graphene, *Proc. Natl. Acad. Sci. USA* **2011**, *108*, 12233.
[55] A. Luican, G. Li, A. Reina, J. Kong, R. R. Nair, K. S. Novoselov, A. K. Geim, E. Y. Andrei, Single-layer behavior and its breakdown in twisted graphene layers, *Phys. Rev. Lett.* **2011**, *106*, 126802.
[56] T. Ohta, J. T. Robinson, P. J. Feibelman, A. Bostwick, E. Rotenberg, T. E. Beechem, Evidence for interlayer coupling and moiré periodic potentials in twisted bilayer graphene, *Phys. Rev. Lett.* **2012**, *109*, 186807.
[57] J. Yin, H. Wang, Z. Tan, L. Liao, L. Lin, X. Sun, A. L. Koh, Y. Chen, H. Peng, Z. Liu, Selectively enhanced photocurrent generation in twisted bilayer graphene with van Hove singularity, *Nat. Commun.* **2016**, *7*, 10699.
[58] C. Cong, T. Yu, S. A. Solin, Enhanced ultra-low-frequency interlayer shear modes in folded graphene layers, *Nat. Commun.* **2014**, *5*, 4709.
[59] R. J. Nemanich, G. Lucovsky, S. A. Solin, Infrared active optical vibrations of graphite, *Solid State Commun.* **1977**, *23*, 117.
[60] M. Mohr, J. Maultzsch, E. Dobardžić, S. Reich, I. Milošević, M. Damnjanović, A. Bosak, M. Krisch, C. Thomsen, Phonon dispersion of graphite by inelastic X-ray scattering, *Phys. Rev. B* **2007**, *76*, 035439.

[61] K. Sato, J. S. Park, R. Saito, C. Cong, T. Yu, C. H. Lui, T. F. Heinz, G. Dresselhaus, M. S. Dresselhaus, Raman spectra of out-of-plane phonons in bilayer graphene, *Phys. Rev. B* **2011**, *84*, 035419.
[62] M. Born, K. Huang, *Dynamical Theory of Crystal Lattices*, Oxford University Press, London, **1998**.
[63] C. H. Lui, Z. Ye, C. Keiser, X. Xiao, R. He, Temperature-activated layer-breathing vibrations in few-layer graphene, *Nano Lett.* **2014**, *14*, 4615.
[64] R. J. Nemanich, G. Lucovsky, S. A. Solin, *Long wavelength lattice vibrations of graphite*, Paris, France, **1977**, pp. 619–621.
[65] S. Sugai, T. Ueda, High-pressure Raman spectroscopy in the layered materials 2H-MoS_2, 2H-$MoSe_2$, and 2H-$MoTe_2$, *Phys. Rev. B* **1982**, *26*, 6554.
[66] P.-H. Tan, J.-B. Wu, W.-P. Han, W.-J. Zhao, X. Zhang, H. Wang, Y.-F. Wang, Ultralow-frequency shear modes of 2-4 layer graphene observed in scroll structures at edges, *Phys. Rev. B* **2014**, *89*, 235404.
[67] H. Zhao, J.-B. Wu, H. Zhong, Q. Guo, X. Wang, F. Xia, L. Yang, P.-H. Tan, H. Wang, Interlayer interactions in anisotropic atomically thin rhenium diselenide, *Nano Res.* **2015**, *8*, 3651.
[68] X.-F. Qiao, J.-B. Wu, L. Zhou, J. Qiao, W. Shi, T. Chen, X. Zhang, J. Zhang, W. Ji, P.-H. Tan, Polytypism and unexpected strong interlayer coupling in two-dimensional layered ReS_2, *Nanoscale* **2016**, *8*, 8324.
[69] M. Miscuglio, M.-L. Lin, F. Di Stasio, P.-H. Tan, R. Krahne, Confined acoustic phonons in colloidal nanorod heterostructures investigated by nonresonant Raman spectroscopy and finite elements simulations, *Nano Lett.* **2016**, *16*, 7664.
[70] A. Girard, L. Saviot, S. Pedetti, M. D. Tessier, J. Margueritat, H. Gehan, B. Mahler, B. Dubertret, A. Mermet, The mass load effect on the resonant acoustic frequencies of colloidal semiconductor nanoplatelets, *Nanoscale* **2016**, *8*, 13251.
[71] X.-L. Liu, H.-N. Liu, J.-B. Wu, H.-X. Wu, T. Zhang, W.-Q. Zhao, P.-H. Tan, Filter-based ultralow-frequency Raman measurement down to 2 cm^{-1} for fast brillouin spectroscopy measurement, *Rev. Sci. Instrum.* **2017**, *88*, 053110.
[72] M.-L. Lin, F.-R. Ran, X.-F. Qiao, J.-B. Wu, W. Shi, Z.-H. Zhang, X.-Z. Xu, K.-H. Liu, H. Li, P.-H. Tan, Ultralow-frequency Raman system down to 10 cm^{-1} with longpass edge filters and its application to the interface coupling in t(2+2)LGs, *Rev. Sci. Instrum.* **2016**, *87*, 053122.
[73] S. K. Saha, U. V. Waghmare, H. R. Krishnamurthy, A. K. Sood, Phonons in few-layer graphene and interplanar interaction: a first-principles study, *Phys. Rev. B* **2008**, *78*, 165421.
[74] J.-W. Jiang, H. Tang, B.-S. Wang, Z.-B. Su, Raman and infrared properties and layer dependence of the phonon dispersions in multilayered graphene, *Phys. Rev. B* **2008**, *77*, 235421.
[75] V. N. Popov, C. Van Alsenoy, Low-frequency phonons of few-layer graphene within a tight-binding model, *Phys. Rev. B* **2014**, *90*, 245429.
[76] H. A. Wilhelm, B. Croset, G. Medjahdi, Proportion and dispersion of rhombohedral sequences in the hexagonal structure of graphite powders, *Carbon* **2007**, *45*, 2356.
[77] K. Yan, H. Peng, Y. Zhou, H. Li, Z. Liu, Formation of bilayer bernal graphene: layer-by-layer epitaxy via chemical vapor deposition, *Nano Lett.* **2011**, *11*, 1106.
[78] Q. Li, H. Chou, J.-H. Zhong, J.-Y. Liu, A. Dolocan, J. Zhang, Y. Zhou, R. S. Ruoff, S. Chen, W. Cai, Growth of adlayer graphene on cu studied by carbon isotope labeling, *Nano Lett.* **2013**, *13*, 486.
[79] R. He, T.-F. Chung, C. Delaney, C. Keiser, L. A. Jauregui, P. M. Shand, C. C. Chancey, Y. Wang, J. Bao, Y. P. Chen, Observation of low energy Raman modes in twisted bilayer graphene, *Nano Lett.* **2013**, *13*, 3594.
[80] V. Carozo, C. M. Almeida, B. Fragneaud, P. M. Bedê, M. V. O. Moutinho, J. Ribeiro-Soares, N. F. Andrade, A. G. Souza Filho, M. J. S. Matos, B. Wang, M. Terrones, R. B. Capaz, A. Jorio, C. A. Achete, L. G. Cançado, Resonance effects on the Raman spectra of graphene superlattices, *Phys. Rev. B* **2013**, *88*, 085401.
[81] R. W. Havener, H. Zhuang, L. Brown, R. G. Hennig, J. Park, Angle-resolved Raman imaging of interlayer rotations and interactions in twisted bilayer graphene, *Nano Lett.* **2012**, *12*, 3162.
[82] P. Moon, M. Koshino, Optical absorption in twisted bilayer graphene, *Phys. Rev. B* **2013**, *87*, 205404.
[83] A. Jorio, M. Kasperczyk, N. Clark, E. Neu, P. Maletinsky, A. Vijayaraghavan, L. Novotny, Optical-phonon resonances with saddle-point excitons in twisted-bilayer graphene, *Nano Lett* **2014**, *14*, 5687.
[84] P. Moon, Y.-W. Son, M. Koshino, Optical absorption of twisted bilayer graphene with interlayer potential asymmetry, *Phys. Rev. B* **2014**, *90*, 155427.
[85] A. S. Davydov, The theory of molecular excitons, *Soviet Physics Uspekhi* **1964**, *7*, 145.
[86] P. Tonndorf, R. Schmidt, P. Böttger, X. Zhang, J. Börner, A. Liebig, M. Albrecht, C. Kloc, O. Gordan, D. R. T. Zahn, S. M. de Vasconcellos, R. Bratschitsch, Photoluminescence emission and Raman response of monolayer MoS_2, $MoSe_2$, and WSe_2, *Opt. Express* **2013**, *21*, 4908.
[87] G. Froehlicher, E. Lorchat, F. Fernique, C. Joshi, A. Molina-Sánchez, L. Wirtz, S. Berciaud, Unified description of the optical phonon modes in n-layer $mote_2$, *Nano Lett.* **2015**, *15*, 6481.
[88] Q. J. Song, Q. H. Tan, X. Zhang, J. B. Wu, B. W. Sheng, Y. Wan, X. Q. Wang, L. Dai, P. H. Tan, Physical origin of davydov splitting and resonant Raman spectroscopy of davydov components in multilayer $MoTe_2$, *Phys. Rev. B* **2016**, *93*, 115409.
[89] M Grzeszczyk, K Gołasa, M Zinkiewicz, K Nogajewski, M R Molas, M Potemski, A Wysmołek, A Babiński, Raman scattering of few-layers $MoTe_2$, *2D Mater.* **2016**, *3*, 025010.
[90] K. Kim, J.-U. Lee, D. Nam, H. Cheong, Davydov splitting and excitonic resonance effects in Raman spectra of few-layer $MoSe_2$, *ACS Nano* **2016**, *10*, 8113.
[91] Q.-H. Tan, X. Zhang, X.-D. Luo, J. Zhang, P.-H. Tan, Layer-number dependent high-frequency vibration modes in few-layer transition metal dichalcogenides induced by interlayer couplings, *J. Semicond.* **2017**, *38*, 031006.
[92] X.-L. Liu, X. Zhang, M.-L. Lin, P.-H. Tan, Different configurations of angle-resolved polarized Raman sepctroscopy: a case on the basal and edge plane of two-dimensional materials, *Chin. Phys. B* **2017**, *26*, 067802.
[93] M.-L. Lin, T. Chen, W. Lu, Q.-H. Tan, P. Zhao, H.-T. Wang, Y. Xu, P.-H. Tan, Rapidly identifying the stacking order of multilayer graphene grown by chemical vapor deposition via Raman spectroscopy, *J. Raman Spectrosc.* **2017**, https://doi.org/10.1002/jrs.5219.
[94] C. H. Lui, T. F. Heinz, Measurement of layer breathing mode vibrations in few-layer graphene, *Phys. Rev. B* **2013**, *87*, 121404.
[95] F. Herziger, P. May, J. Maultzsch, Layer-number determination in graphene by out-of-plane phonons, *Phys. Rev. B* **2012**, *85*, 235447.